AFRL-RH-FS-TR-2023-0006

Broadband Optical Constants Measurement Device

Alexander P. Greis
Nanohmics Inc.

Joel N. Bixler
711th Human Performance Wing
Airman Systems Directorate
Bioeffects Division
Optical Radiation Branch

March 2023

Interim Technical Report for February 2022 – February 2023

DESTRUCTION NOTICE – Destroy by any method that will prevent disclosure of contents or reconstruction of this document.

Air Force Research Laboratory
711th Human Performance Wing
Airman Systems Directorate
Bioeffects Division
Optical Radiation Bioeffects Branch
JBSA Fort Sam Houston, Texas 78234

NOTICE AND SIGNATURE PAGE

Using Government drawings, specifications, or other data included in this document for any purpose other than Government procurement does not in any way obligate the U.S. Government. The fact that the Government formulated or supplied the drawings, specifications, or other data does not license the holder or any other person or corporations; or convey any rights or permission to manufacture, use, or sell any patented invention that may relate to them.

This report was cleared for public release by the AFRL Public Affairs Office and is available to the general public, including foreign nationals. Copies may be obtained from the Defense Technical Information Center (DTIC) (http://www.dtic.mil).

"Broadband Optical Constants Measurement Device "

(AFRL-RH-FS-TR- 2023- 0006) has been reviewed and is approved for publication in accordance with assigned distribution statement.

GOETTL.BARRY.P.1229728977 Digitally signed by GOETTL.BARRY.P.1229728977 Date: 2023.04.05 07:36:31 -05'00'

BARRY P. GOETTL, PhD
Acting Chief, Optical Radiation Bioeffects Branch

MILLER.STEPHANIE.A.1230536283 Digitally signed by MILLER.STEPHANIE.A.1230536283 Date: 2023.04.20 17:09:06 -05'00'

STEPHANIE A. MILLER, DR-IV, DAF
Chief, Bioeffects Division
Airman Systems Directorate
711th Human Performance Wing
Air Force Research Laboratory

This report is published in the interest of scientific and technical information exchange, and its publication does not constitute an official position of the U.S. Government.

REPORT DOCUMENTATION PAGE

Form Approved
OMB No. 0704-0188

1. REPORT DATE *(DD-MM-YY* **2.** *10-3-2023*	**2. REPORT TYPE** Interim Technical Report	**3. DATES COVERED** *(From - To)* 10 February 2022 – 29 December 2022

4. TITLE AND SUBTITLE

Broadband Optical Constants Measurement Device

5a. CONTRACT NUMBER
FA8650-19-C-6024

5b. GRANT NUMBER

5c. PROGRAM ELEMENT NUMBER

6. AUTHOR(S)

Alexander Greis

5d. PROJECT NUMBER

5e. TASK NUMBER

5f. WORK UNIT NUMBER
H14B

7. PERFORMING ORGANIZATION NAME(S) AND ADDRESS(ES)
Nanohmics, Inc
6201 E. Oltorf St., STE. 400
Austin, TX 78741

8. PERFORMING ORGANIZATION REPORT

9. SPONSORING / MONITORING AGENCY NAME(S) AND ADDRESS(ES)
711th Human Performance Wing
Airman Systems Directorate
Bioeffects Division
Optical Radiation Branch
JBSA, Fort Sam Houston, Texas 78234

10. SPONSOR/MONITOR'S ACRONYM(S)
711 HPW/RHDO

11. SPONSOR/MONITOR'S REPORT NUMBER(S)
AFRL-RH-FS-TR-2023-0006

12. DISTRIBUTION / AVAILABILITY STATEMENT

DISTRIBUTION STATEMENT A: Approved for public release; distribution in unlimited. CLEARED: PA Case # AFRL-2023-1904.The views expressed are those of the author and do not necessarily reflect the official policy or position of the Department of the Air Force, the Department of Defense, or the U.S

13. SUPPLEMENTARY NOTES

14. ABSTRACT

During the STTR Phase II program, Nanohmics designed and implemented prototype instrumentation – the Broadband Optical Characterization System (BOCS) – for the measurement of optical and thermal material properties of biological tissue. Fundamental to the device design is a large reflective optical element that enables measurement of the bidirectional scatter distribution function (BSDF) at video rates. A Python post-processing software suite –BOCS Analysis – applied to the captured BSDF imagery enables estimation of the scattering coefficient, absorption coefficient, Henyey-Greenstein scattering anisotropy factor, and extinction coefficient. Through integration of a tunable source and automation of instrumentation and temperature control hardware, the BOCS can readily characterize tissue samples as a function of wavelength, temperature, or during dynamic events such as high energy laser (HEL) exposure.

15. SUBJECT TERMS
STTR, BRDF BTDF measurement, optical scatter, optical absorption, tissue optical properties, tissue thermal properties

16. SECURITY CLASSIFICATION OF: Unclassified			**17. LIMITATION OF ABSTRACT**	**18. NUMBER OF PAGES**	**19a. NAME OF RESPONSIBLE PERSON** Joel N. Bixler
a. REPORT U	**b. ABSTRACT** U	**c. THIS PAGE** U	NA	72	**19b. TELEPHONE NUMBER** *(include area code)* 210-539-8172

Standard Form 298 (Rev. 8-98)
Prescribed by ANSI Std. Z39.18

TABLE OF CONTENTS

Section		Page
List of Figures		ii
List of Tables		iii
1.0	EXECUTIVE SUMMARY	1
2.0	INTRODUCTION	1
3.0	METHODS, ASSUMPTIONS, AND PROCEDURES	2
4.0	RESULTS AND DISCUSSION	17
5.0	CONCLUSIONS	22
6.0	REFERENCES	23
LIST OF SYMBOLS, ABBREVIATIONS, AND ACRONYMS		24

LIST OF FIGURES

		Page
Figure 1.	BOCS primary measurement system architecture and	2.
Figure 2.	Damaged Phase II paraboloidal mirror and new paraboloidal mirror	3.
Figure 3	Simulation results indicating beam spread versus AOI	3.
Figure 4	Beam BTDF at varying AOI configurations	4.
Figure 5	Rotation of BTDF signal to compensate for non-normal beam AOI	5.
Figure 6	Simulated reflectance of the BOCS beam splitter	7.
Figure 7	BRDF Calibration at 600 nm, 800 nm, and 1000 nm	8.
Figure 8	Typical power meter spectral calibration curve and beam width calibration	9.
Figure 9	BOCS detection ray tracing trajectories for a scattering media and point source	12.
Figure 10	ARS datasets generated from MCSLinv convergence testing	13.
Figure 11	Seventh iteration MCSLinv optimization likelihood	13.
Figure 12	Simulation of the BOCS iris rejection of out-of-focus light	14.
Figure 13	Experimental and synthetic Biomimic ARS datasets	15.
Figure 14	Brewster angle measurement and fit to the Fresnel reflectance equation	17.
Figure 15	Polarimetric BRDF measurement data for the 70% reflectance standard	18.
Figure 16	Multispectral BRDF measurements of the Spectralon reflectance standard	18.
Figure 17	Measured ND filter absorbance, transmittance, and reflectance data	19.
Figure 18	Henyey-Greenstein scattering anisotropy validation data	21.
Figure 19	Biomimic tissue phantom refractive index measurement data	22.

LIST OF TABLES

Page

Table 1 INO Biomimic OP-HBO-C-940-0.65-5 Tissue Phantom properties..... 20.

1.0 EXECUTIVE SUMMARY

Nanohmics, Inc., hereby referred to as Nanohmics, has continued the development of prototype instrumentation called the Broadband Optical Characterization System (BOCS) for the measurement of optical and thermal material properties of biological tissues. Fundamental to the device design is a large reflective optical element that enables measurement of the bidirectional scatter distribution function (BSDF) at video rates. A Python (Python Software Foundation) post-processing software suite called BOCS Analysis enables estimation of the scattering coefficient, absorption coefficient, Henyey-Greenstein scattering anisotropy factor, and refractive index when applied to the captured BSDF imagery. Through integration of a tunable source and automation of instrumentation and temperature control hardware, the BOCS can readily characterize tissue samples as a function of wavelength, temperature, or during dynamic events such as high energy laser (HEL) exposure.

2.0 INTRODUCTION

This document summarizes improvements made to the BOCS and presents validation measurements performed under this effort. The objective of performing these measurements has been to demonstrate system measurement performance on materials with known parameters, improving confidence in measurement data in preparation for experimentation on tissue samples with unknown material properties.

The BOCS is an optical measurement system designed to characterize *ex vivo* biological tissue sample optical properties as a function of wavelength, of temperature, and of time (during dynamic events). The fundamental measurement performed by the BOCS is that of the simultaneous bidirectional reflectance distribution function (BRDF) and bidirectional transmittance distribution function (BTDF), which together comprise the BSDF. This measurement is facilitated via use of a large parabolic mirror into which the sample is inserted, which enables remapping of the angular scatter distribution into a Cartesian coordinate system that is measured with a camera (Panda 42 bi, PCO). Material optical properties including the Henyey-Greenstein anisotropy factor, scattering and absorption coefficients, and refractive index are then calculated from the measured BSDF.

Figure 1 provides a high-level diagram of components within the optical system. The sample (A) is inserted within the parabolic mirror (B) and illuminated with a probe beam (C), the power of which is measured via use of a pickoff mirror and optical power meter (F). Reflected and transmitted light – containing the sample's BSDF signal – is focused onto an iris (D) for rejection of uncollimated light and imaged by a camera (E). Another pickoff mirror and optical power meter (G) are used to estimate the sample's absorption fraction, and a HEL (H) may optionally be used to heat the sample for dynamic studies, in which case a line-blocking filter (I) is installed at the output of the system to enable separation of the probe source from the HEL.

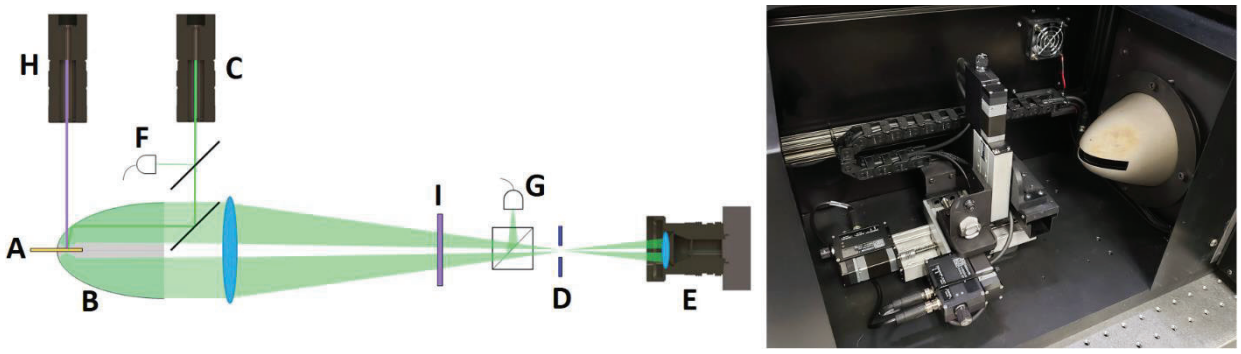

Figure 1. BOCS primary measurement system architecture and photograph

During this effort many improvements were made to the BOCS, and a subset of the measurement capabilities have been validated on limited sample sets. However, unexpected complications with the technique used for estimation of the material scattering and absorption coefficients prevented arose during this effort and prevented completion of the system validation.

3.0 METHODS, ASSUMPTIONS, AND PROCEDURES

Numerous changes have been made to the BOCS instrument under this effort, many of which were designed to address performance limitations identified during the Phase II program. Major changes to the system are discussed below, although other minor changes have been implemented including improved coupling between the tunable source (TLS-72-X300, ScienceTech) and the BOCS hardware, addition of an adjustable iris for control of probe beam width, fabrication of 3D printed alignment assistance tools, and a variety of software features concentrated on improving the repeatability and ease of sample focusing and alignment.

The paraboloidal mirror procured during the Phase II was determined to have several large defects, resulting in missing or incorrect angular mapping of the signal to the focal plane array (FPA). Near the end of the Phase II program, it was hypothesized – through simulation and discussions with the vendor (Optiforms, Inc.) – that the paraboloid was damaged due to either the electrical discharge machining process of the cutout features or through improper handling. A replacement paraboloid was procured and installed. Figure 2 shows images of the damaged paraboloid and replacement under illumination with a Lambertian reflectance standard installed in the sample port. No major defects are present in the new paraboloid, although a mid-spatial frequency pattern can still be observed due to the vendor's stated tolerance of 7λ at 632 nm. Given that these paraboloidal mirrors are electroformed from a master mandril, improvement upon this form would require machining a new mandrel. This approach may be pursued in the future if it is determined that the mirror is limiting performance, but during this effort the calibration of the paraboloid using Lambertian scattering materials proved acceptable for measurement requirements.

Figure 2. Damaged Phase II paraboloidal mirror and new paraboloidal mirror

Sample absorption fraction is estimated using the ratio of measured power from two optical power meters (PM16-120, Thorlabs), one located at a pickoff near the probe beam input and the other at the output of the paraboloid. After calibration, the ratio between the output power and input power is used to estimate sample absorbance. However, during Phase II it was observed that the instrumentation overestimated absorption fraction at steep probe beam angles of incidence. Due to the system's finite beam size, the beam profile at the sample plane becomes elliptical at steep angles of incidence, resulting in a wider beam spread at the collection aperture of the output power meter. Figure 3 illustrates confirmation of this behavior with simulated results and experimental data.

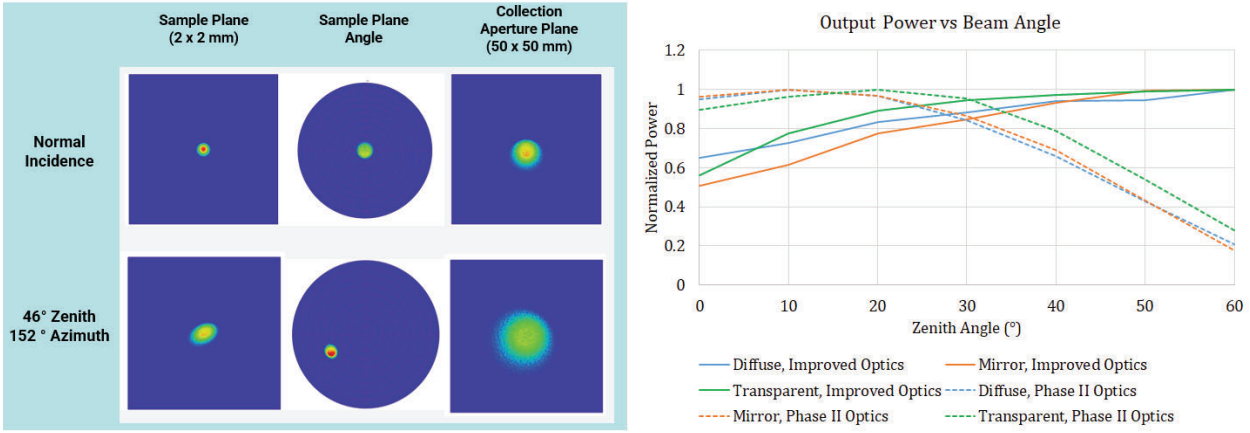

Figure 3. Simulation results indicating beam spread versus AOI

To mitigate this issue, the existing one-inch diameter collection optics for the output power meter were replaced with three-inch diameter optical components, increasing the effective collection region at the pickoff. This new collection system was installed immediately before the imaging system enclosure and fabricated using a 3D-printed mounting apparatus, a large beam-splitter (TED Pella), and a large plano-convex collection lens (LA1353, Thorlabs). Improvements made to the collection efficiency at steep angles was verified by measuring the power of three samples (a polymer diffuser sheet, a mirror, and a transparent microscope slides) at varying angles of incidence with both the original and improved optical configuration. As seen in Figure 3, the measured power in the previous optical configuration declined as the angle of incidence (AOI) was increased, whereas the behavior in the improved configuration does not decrease. The

normalized power in the new configuration increases slightly as a function of AOI, since at normal incidence much of the input beam is lost through the HEL access port (this behavior can be seen to a lesser extent in the original configuration as well).

An improved camera system was provided to Nanohmics by Air Force Research Laboratory (AFRL) personnel to facilitate measurements in the near-infrared (NIR) band for the planned tissue studies. The previous camera system used for BRDF measurement (TM-4100CL, Pulnix) featured a CCD (KAI-4021, Kodak) that had minimal quantum efficiency in the spectral bands of interest (including 1064 nm). As such, a NIR-enhanced camera (panda 4.2 bi, PCO) was procured and installed in the BOCS. This camera features a sCMOS focal plane array (FPA) (GSENSE2020BSI, GPixel) that not only has appropriate sensitivity in the desired spectral bands but also improved dynamic range, analog-to-digital converter (ADC) resolution, and framerates compared to the previous camera system.

The motion control software has been augmented to allow users (and automated routines) to specify the polar coordinates in azimuth (φ) and zenith (θ) of the incidence angle at the sample plane. The accuracy of this routine has been validated via observation of the BTDF of the beam with no sample, as seen in Figure 4. This has enabled the implementation of much improved calibration methods for the refractive index measurements, in which the beam must be positioned at varying AOI.

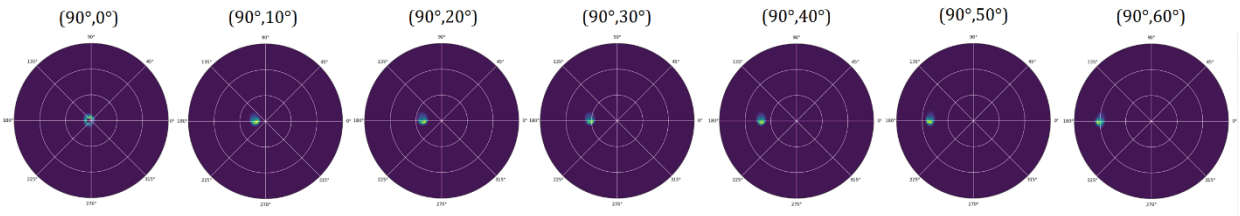

Figure 4. Beam BTDF at varying AOI configurations

Knowledge of the probe beam AOI enables rotation of the spherical coordinate system about the paraboloidal mirror's focal point to adjust for non-normal beam AOI. This is useful for measurements where data lost due to the presence of the HEL access port prevents collection of important angular ranges, such as with measurement of the scattering and absorption coefficients or scattering anisotropy. Addition of a rotation transform has enabled measurement of the BSDF at slight offsets from normal (≈ 6.0°) for such purposes. In Figure 5, the BTDF of a Biomimic tissue phantom with beam AOI set to (90°,11°) (azimuth, zenith) as measured (left) and after rotation (center) is shown. The radial average of both signals (right) illustrates reduction of the missing signal near 180˚ (original beam propagation direction).

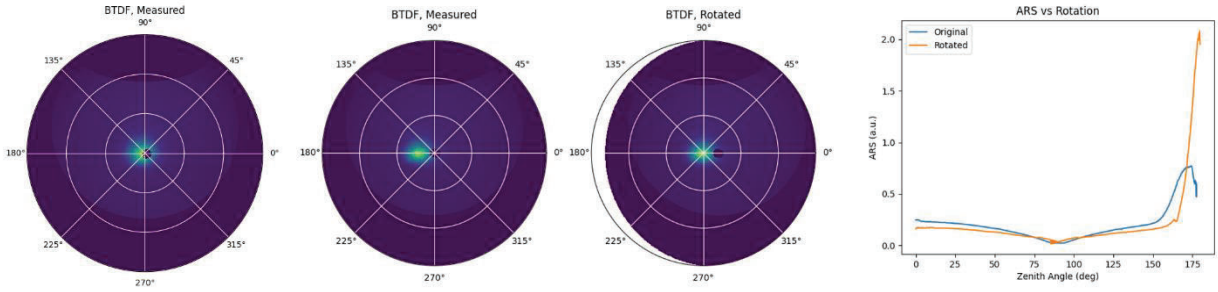

Figure 5. Rotation of BTDF signal to compensate for non-normal beam AOI

3.1. Calibration Method Improvements

The BOCS calibration process includes measurements of spectral BSDF mapping to the camera sensor as well as characterization of the reference power measurements to the input beam. This process has been automated using a custom calibration cartridge and computer-controlled positioning systems for both the sample and beam positioning (controlling the angle of incidence at the sample plane). Recalibration of the system is only necessary if the alignment is modified or if changes are made to the beam size (through adjustment of an iris positioned immediately after the collimation optics for the probe beam fiber input), the iris diameter at the confocal point, or the tunable source power setting. However, since the calibration process is automated and completes in under ten minutes this has been performed at the beginning of each day measurements were performed. Results shown in this section are typical results representative of all calibration datasets.

The polar mapping calibration is performed via identification of the origin coordinates for both the reflected and transmitted domains. The laser thermal source access hole provides a convenient feature for identification of these origin points, since it has been machined at the normal vector from the sample plane. For the reflected domain, a well illuminated image of a Lambertian scatterer (Spectralon, Labsphere) enables identification of the access hole. Similarly, when the instrument is configured with the beam at normal incidence and no sample inserted a ring-shaped beam is observed, which provides obvious features for identification of the transmitted domain origin.

Once these two points are identified, the unique pixel to angular domain coordinate mapping is established with knowledge of the known paraboloid geometry. This conversion is achieved through use of equations 1-4 below, which are derived from geometric relationships described by Ren et al. [1] These equations define azimuth (φ) and zenith (θ) as a function of paraboloid focal length (f) and normalized exit aperture coordinates (x, y). The identified center coordinates provide an offset (o_x, o_y) and magnification factor (m) to account for lateral misalignment of the system as well as the magnification factor between the paraboloid's output aperture and the size of the image upon the camera sensor.

$$\theta = \cos^{-1}\left(\frac{4fy_c}{4f^2 + \sqrt{{x_c}^2 + {y_c}^2}}\right) \quad (1)$$

$$\varphi = \begin{cases} \tan^{-1}\left(\frac{4f^2 - {x_c}^2 - {y_c}^2}{4fx_c}\right), & x_c > 0 \\ \tan^{-1}\left(\frac{4f^2 - {x_c}^2 - {y_c}^2}{4fx_c}\right) + \pi, & x_c < 0 \\ \frac{\pi}{2}, & x_c = 0,\ y_c < f \\ -\frac{\pi}{2}, & x_c = 0,\ y_c > f \end{cases} \quad (2)$$

$$x_c = x * m + o_x \quad (3)$$

$$y_c = y * m + o_y \quad (4)$$

A valid image mask is generated from the same origin coordinates identified for the polar remapping calibration. This mask is generated using the known paraboloid geometry and the spacing between the reflected and transmitted domain origin coordinates as viewed from the exit aperture of the paraboloid. This mask eliminates any image regions not within the valid paraboloid boundaries and excludes them from analysis.

A correction factor is applied to the reflected domain to accommodate for losses due to the presence of the beam splitter in the BRDF-portion of the signal, as seen in Figure 1. This correction factor was determined via simulation (using Zemax OpticStudio version 19.4 SP2) of a collimated beam interacting with the beam splitter (260454, TED Pella), using the vendor provided thickness and material (Schott D263 borosilicate glass). A polynomial equation was fit to the simulated spectral transmittance of the beam splitter, as seen in Figure 6. During measurement, the scalar transmittance value is used to adjust the reflected domain signal magnitude.

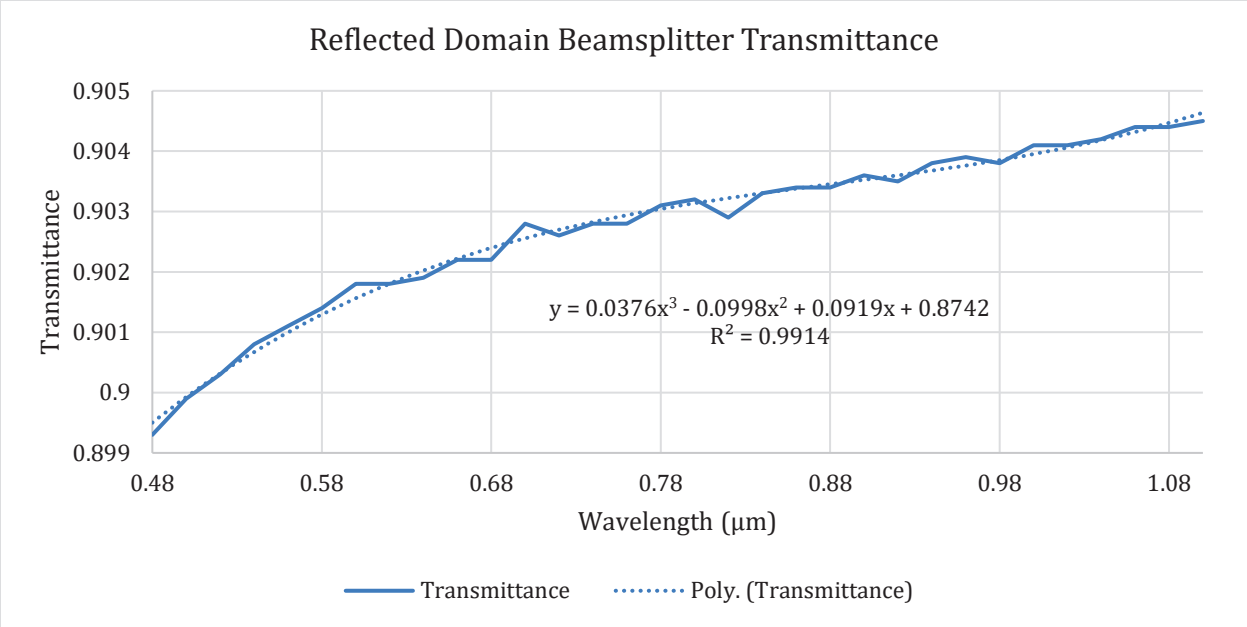

Figure 6. Simulated reflectance of the BOCS beam splitter

The polar data produced by the remapping of the image sensor data is converted into BRDF by comparison of instrument measurements of a NIST-traceable reflectance standard to the known values reported by the vendor (Spectralon, Labsphere). The correction factor is generated for each pixel in the FPA with known polar coordinates (azimuth φ and zenith θ), across the 450 nm to 1100 nm spectral band in 10 nm intervals, and the correction factor is interpolated from the measured dataset at intermediate wavelengths.

As seen in equation 5, the BRDF of an arbitrary sample (f) is expressed as the ratio of the measured sample radiant flux (Φ_r) and the measured radiant flux of a Lambertian reflectance standard (Φ_o) scaled by the known Lambertian reflectance. In the BOCS system, the spectral reflectance (R) of the calibration sample has been provided by the vendor (Labsphere, Inc.). These parameters are expressed as a function of the incident and reflected azimuth and zenith ($\varphi_i,\theta_i;\ \varphi_r,\theta_r$), however the BRDF is also dependent on the wavelength, polarization state, beam power, and system iris size. These terms have been left out in equation 5 for simplicity, but in practice each variation of beam size, power, iris size, and wavelength require separate calibration. Note that the original definition of BRDF by Nicodemus *et al.* includes parameters for the detector solid angle and total incident radiance. By ratioing the calibration and sample measurements these terms are not explicitly required, provided the measurement configuration is the same between the two measurements.

$$f(\varphi_i,\theta_i;\varphi_r,\theta_r) = \frac{R}{\pi}\frac{\Phi_r(\varphi_i,\theta_i;\varphi_r,\theta_r)}{\Phi_o(\varphi_i,\theta_i;\varphi_r,\theta_r)} \quad \textbf{(5)}$$

There are several important assumptions and limitations of this calibration technique. A primary limitation of the system calibration is that the BRDF is reflected over the paraboloid centerline and applied to BTDF. While this is not ideal, there exist no readily available BTDF standards amenable

to use in the BOCS. Procurement and characterization of such a standard would provide improved confidence in the transmitted domain measurements. Regarding the truth values used for the BRDF correction, data provided from the vendor was performed using under broadband illumination with a Tungsten-Halogen lamp and is assumed to be invariant with wavelength across the relevant spectral bands. Additionally, the BRDF correction factor is only valid under the same illumination angle, field aperture size, and camera integration time(s). As such, the BOCS should be calibrated in the same configuration as the subsequent experiments. It is worth noting that within the BOCS instrumentation the beam size at the sample plane does change due to the collimation optics in the source assembly and influences this correction factor. This effect can be reduced by reducing the beam size via adjustment of an iris in the source optics but presents a tradeoff with delivered power, which can be critical for measuring transmitted signal through thick samples. Some of these limitations could be removed by automating calibration across all incidence angles, iris sizes, and camera exposure times. However, implementation of such an exhaustive parameter space has thus far been determined unnecessary and would be time and data-storage intensive.

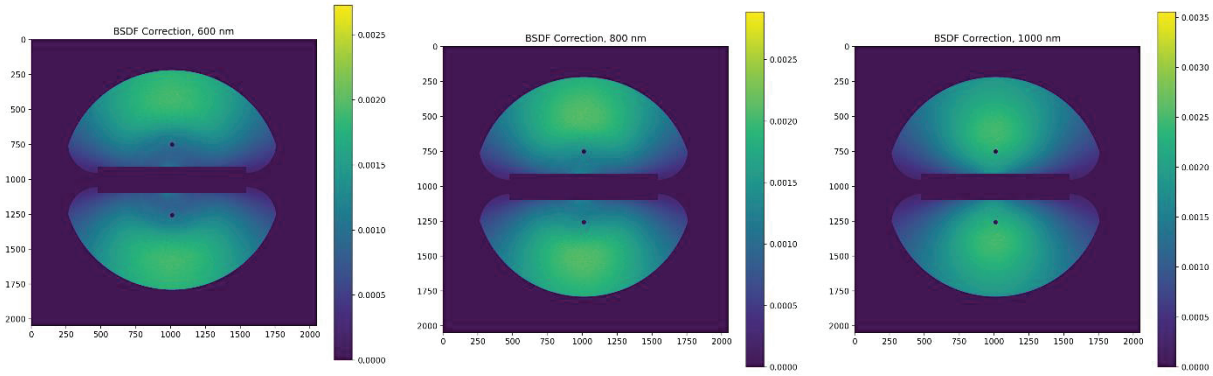

Figure 7. BRDF Calibration at 600 nm, 800 nm, and 1000 nm

Absorbance measurements in the BOCS are based upon the ratio of two power meters (PM16-120, Thorlabs) installed within the system - one immediately at the source input and the other near the system focus (i.e., the remaining power in the reflected and transmitted signal after the beam interacts with the sample). The same reflectance standard used for the BRDF calibration was provided with NIST-traceable reflectance data from the vendor, and as such is used to calibrate the absorption measurements. This calibration assumes that the absorbance, transmittance, and reflectance sum to one and the reflectance standard has no transmittance. The reflectance standard is measured across the 480 nm to 1100 nm spectral band and the resulting calibrated power ratio (P_{oc}/P_{ic}) and vendor reported reflectance data (R_{spec}) is applied to subsequent measured sample power ratios (P_{os}/P_{is}) to estimate sample absorbance (A) according to equation 6. A typical power ratio calibration dataset can be seen in Figure 8.

$$A(\lambda) = 1 - \frac{P_{os}(\lambda)}{P_{is}(\lambda)} \frac{P_{ic}(\lambda)}{P_{is}(\lambda)} R_{spec}(\lambda) \tag{6}$$

Several limitations of this technique have been identified and must be considered when configuring the BOCS for measurement. When measuring highly absorptive or thick samples there is low available output power – especially at longer wavelengths where the power meter quantum efficiency is relatively poor. This comprises a fundamental limitation of the instrumentation and should be considered when selecting and preparing samples for measurement. Another limitation is related to the incomplete sampling of the reflected and transmitted signals due to the missing angular regions in the paraboloidal mirror. With near-normal beam incidence angles this typically contributes only a small error and is already considered for the Lambertian scatter case with the reflectance standard calibration. However, if a steep beam angle is used it is critical that the beam is oriented such that the transmitted and reflected beams are not directed to the uncollected regions, which can potentially result in overestimation of the sample absorbance, since light that does not impinge upon the paraboloidal mirror will be considered absorbed.

Calibration of the beam width is necessary for the estimation of sample reflectance to discriminate the specular component from backscattered light. No sample is installed within the paraboloidal mirror during this calibration process and the source wavelength is scanned from 480 nm to 1100 nm, generating images of the beam width in the transmitted domain. The resulting signal is binarized using Otsu's method and the angular extent of the masked beam region is recorded. A typical beam width calibration curve is shown in Figure 8. Note that the beam width can be adjusted to provide a smaller or larger beam, making a tradeoff with available power.

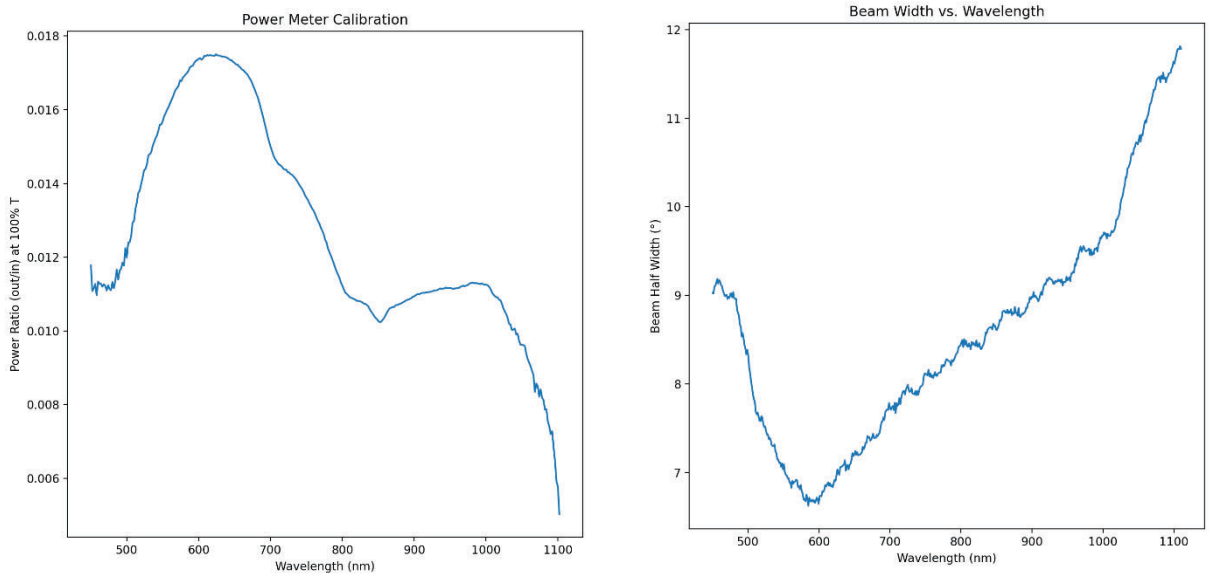

Figure 8. Typical power meter spectral calibration curve and beam width calibration

As can be seen, even with use of a collimation optic designed for a center wavelength of 950 nm the minimum beam divergence is observed around 600 nm. This is largely explained by the chromatic focal length shift refractive optics in the light collection system. The BRDF camera imaging lens (AC300-100-B, Thorlabs) features less than 20 μm of chromatic focal shift across the bands of interest, however it expected that the largest contributor to this is the large primary optic (1200 mm air-spaced achromat, Wollensak). Unfortunately, information on this lens's

chromatic performance is unavailable as the original manufacturer has ceased operations. In subsequent reflectance measurements, a region of interest (ROI) for the probe beam wavelength is interpolated from the calibrated angular beam width, which can be used to estimate specular reflectance via the ratio of integrated energy within this ROI to the transmitted domain.

3.2. Scattering and Absorption Coefficient Estimation

BOCS estimation of μ_a and μ_s' is achieved by inputting measurement data into MCSLinv v 1.0 (https://github.com/usnistgov/MCSLinv), an open-source software package released by Levine *et al.* [2, 3] from the National Institute of Standards and Technology (NIST). MSCLinv implements an inversion method for determination of unknown optical scattering parameters of turbid media and is based upon iterative minimization of the residual error between experimental data and those synthesized by a Monte-Carlo based raytracing method for a given set of optical scattering parameters. To leverage this software, the BOCS BSDF data is reduced to a compatible angle-resolved scattering (ARS) format described by the authors of MCSLinv and known material properties, including the refractive index, scattering anisotropy factor, and thickness are defined prior to performing the inversion method.

The accuracy of this approach was evaluated upon receipt of a calibrated tissue phantom (Biomimic OP-HBO-C-940-0.65-5, INO). However, initial reported values for scattering and absorption coefficients were not in agreement those reported by the vendor, instigating a detailed investigation into the measurement approach. To the reduce the complexity of the measurement configuration and isolate potential discrepancies in assumptions and methods, the tissue phantom was measured in a sample holder that features no coverslip on either side of the sample, eliminating any additional reflections or ghost images. Investigations thus far have focused upon the same wavelength (940 nm) as the vendor-reported calibration data.

One potential source of error identified was that the BOCS features missing angular regions due to the HEL port in the paraboloidal mirror, resulting in lost signal near the zenith in the reflected domain. If the incident beam angle is configured for normal incidence a large portion of the incident beam is lost as well, resulting in a ring-shaped beam profile and loss of the same angular region in the transmitted domain. To prevent evaluation of these regions in material property estimation, the BOCS processing software applies an ROI mask to the recorded imagery, removing angles near the zenith from subsequent analysis. However, MCSLinv assumes a measurement configuration like that of the NIST's Spectral Tri-function Automated Reference Reflectometer (STARR), which does not feature such missing angular regions.

The synthetic data generated by the forward Monte-Carlo raytracing features data from the entire polar sphere about the sample, and, when compared to the BOCS data with the missing regions, incorrectly reduces the residual error by increasing the absorption coefficient. To address this issue, a stepped weighting function was added to the scoring of synthetic data to remove the angular regions corresponding to the HEL port. In the search loop of the inversion method, each combination of μ_a and μ_s' is scored by calculating the log likelihood (L) of the synthetic dataset generated with the specified parameters ($ARS_{s,n}$) and the experimental data ($ARS_{e,n}$) across all N samples, as shown in equation 7. This function is adjusted to remove the first and last region by selecting N from 1 to N-1. While the weighting function addition did improve the accuracy of the

estimated results it did not result in estimation of the correct material scattering and absorption coefficients.

$$L = \frac{N}{2}\log\frac{\sum_{n=0}^{N}\left(ARS_{e,n} - ARS_{s,n}\right)^2}{N} \quad (7)$$

Another source of error in the initial results stem from the assumption within MCSLinv that all rays that are not absorbed by the sample are collected by the measurement system. In the BOCS measurement configuration light exiting the sample may be lost due to the paraboloid's HEL port, cartridge insertion cutout, or exit aperture. Light exiting the sample away from the focus (due to bulk scattering within the sample) may be blocked by the system iris or in miss the primary focusing lens. In the original MCSLinv code, the only mechanism by which to accommodate for these losses in the experimental data was to increase the estimated absorption coefficient. To correct for this discrepancy, the MCSLinv code was modified via implementation of a raytracing method that receives the last direction vector and position of rays prior to detection and determines if they are collected or attenuated within the BOCS hardware configuration. A separate weighting scheme was also added to remove attenuated rays from detection and subsequent log likelihood scoring without altering other aspects of the optical property weighting.

In the added detection raytracing methods three components of the BOCS hardware are considered: the paraboloidal mirror, the primary objective, and the iris. The intersection of exiting rays from the sample with the mirror is found via substitution of the parameterized line equation (corresponding to the ray) into the paraboloid surface equation. If the ray intersects the mirror at the HEL port, cartridge cutout, or passes directly to the output aperture it is not collected, otherwise the ray direction vectors are reflected over the surface normal of the paraboloidal mirror and propagated to the focusing objective, noting that the relative position of the elements is the same as the hardware configuration. If rays land outside of the lens aperture they are not collected, otherwise their direction vector is changed according to the thin-lens approximation (d=127 mm, f = 1200 mm) since the exact prescription of the lens is not known. Finally, the parameterized line equation for each ray is traced to the z-coordinate (along the optical axis) of the iris. If the ray intersects this plane within the iris diameter used in the experiment it is collected, otherwise it is attenuated. All these functions have been implemented as C code within MCSLinv and do not significantly increase the time of the simulation, as the scattering simulation within the sample involves many more interaction events. The output of this software function is binary detection result for each ray, but illustrative ray trace plots – as seen in Figure 9 – demonstrate performance consistent with empirical results and Zemax simulation.

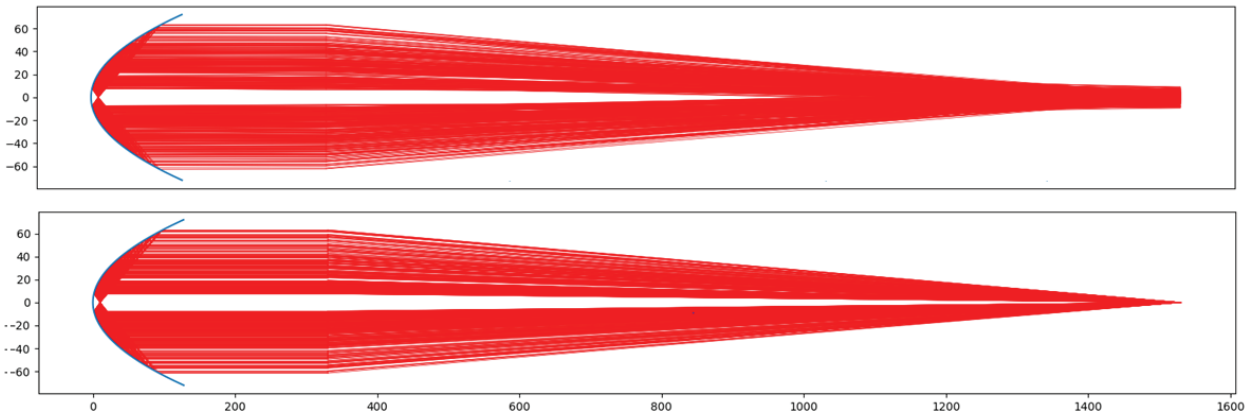

Figure 9. BOCS detection ray tracing trajectories for a scattering media and point source

Using this BOCS detection method requires knowledge of the focal point depth within the tissue sample, as the BOCS hardware is highly sensitive to the position of the sample within the paraboloid. As such, focal depth/position has been added as an additional input into the MCSLinv software. The current practice when performing measurements with the BOCS is to focus upon the middle of the sample in the beam axis. This is achieved by translating the sample such that the top surface is in focus – maximizing the total integrated BRDF – and then recording this position. The same process is repeated for the BTDF, and then the middle point between the two surfaces is used for experimental measurements.

Other aspects of the BOCS μ_a and μ_s' estimation methods were investigated, but changes made during these investigations were ultimately determined unnecessary or invalid. Beam angular and spatial distribution functions based upon measurement data were implemented, which configured the starting coordinates and direction vectors of rays in the MCSLinv simulation to be representative of the BOCS hardware. However, addition of this beam distribution instigated dramatic overestimation of the scattering coefficient, which is to be expected given that the BSDF estimation effectively removes the beam size and shape (but is only valid for the beam configuration used in the calibration). An alternative method of generating the BSDF was also implemented but yielded similar results. In this method, the solid angle subtended by each pixel (Ω_n) was calculated using the polar angle remapping calibration, and the subsequent BSDF assigned to each pixel ($f(n)$) was that pixel's measured radiant flux (Φ_n) divided by the total image radiant flux ($\Sigma\Phi$), scaled by the measured ratio of unabsorbed light ($1\text{-}A$), as seen in equation 8.

$$f(n) = (1 - A)\frac{\Phi_n}{\Omega_n \sum \Phi} \tag{8}$$

Convergence testing was performed on the original and modified MCSLinv, which features the updated weighting and BOCS detection raytracing component. To perform this test, a synthetic dataset was generated using the known material properties and used as input into the MCSLinv inverse method. The results produced by both configurations matched the original synthetic ARS dataset with total residual error of less than 0.2%, as seen in Figure 10.

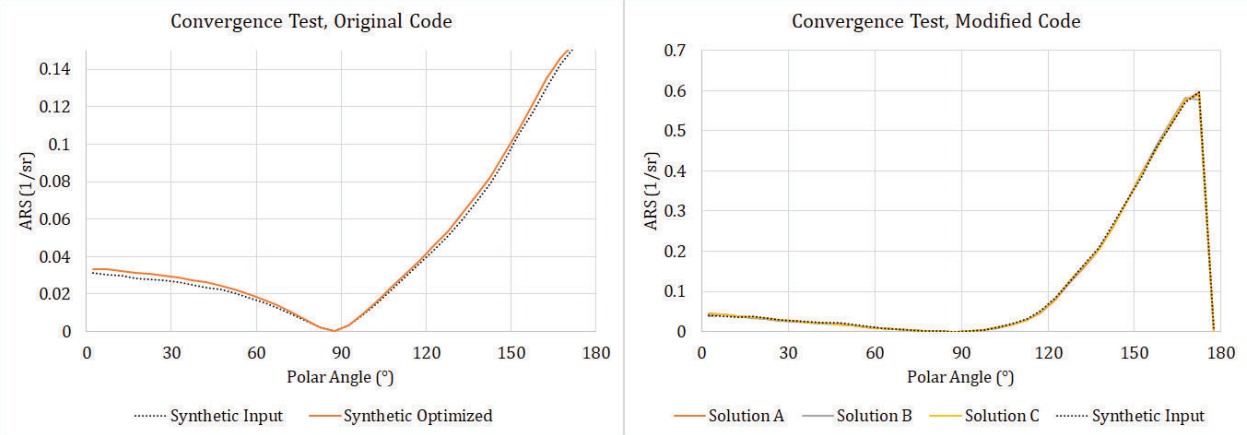

Figure 10. ARS datasets generated from MCSLinv convergence testing

The modified MCSLinv does not currently converge to the same values of μ_a and μ_s' with repeated executions of the inversion methods for the same input parameters. As illustrated in Figure 10, the original code always converges to the same optical parameters used to generate the input data (within the tolerances implicit in the search parameters). However, the modified MCSLinv will converge to different combinations of parameters. The three solutions shown in the Figure 10 correspond to (μ_a ,μ_s') values of (2.10 cm^{-1}, 3.92 cm^{-1}), solution B is (2.44 cm^{-1}, 4.09 cm^{-1}) and solution C is (1.32 cm^{-1}, 3.75 cm^{-1}). Further investigation revealed that the likelihood map for the inversion method does not feature a unique solution and that the reported values lie along a valley, as seen in Figure 11. Note that the search grid is defined in terms of μ_t and η_a, where $\mu_t = \mu_a + \mu_s$ and $\eta_a = \mu_a/(\mu_a + \mu_s)$. The original MCSLinv software converges to a unique solution, whereas the current modified code does not.

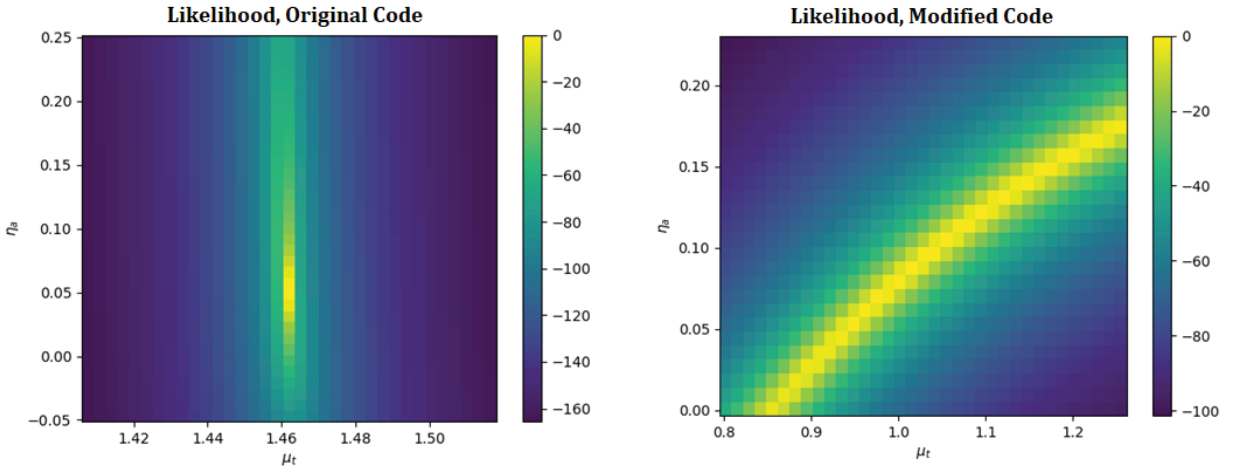

Figure 11. Seventh iteration MCSLinv optimization likelihood

Removal of the weighting function from the likelihood calculation methods indicates that the behavior shown in Figure 11 is due to the added BOCS detection raytracing methods. Increasing the number of simulated rays, iterations, and reducing the allowable tolerance in the search did not

improve the repeatability. Attenuation of out-of-focus light by the BOCS optical system may potentially provide a partial explanation for this behavior. The BOCS system iris is designed to attenuate light that is not collimated, since all light exiting from the system focus is nominally collimated at the mirror output. An adjustable iris (0-25 mm in diameter) allows selection of the acceptance region around the focus. Bulk scattering within the sample can cause rays to be rejected if they exit the sample media at sufficient distance from the focal point. Similarly, samples with finite thickness will produce poorly collimated light which may be rejected at the output depending on the iris configuration and sample properties. In Figure 12 this behavior is shown with a synthetic dataset. Three elliptical sources with angular span of ±25° centered at the zenith are positioned at the paraboloidal mirror focus (blue), displaced 1 mm in the y-axis (green), and 1 mm in the z-axis (red). As can be seen, the focused source is completely collected, whereas the displaced ones are not. Note that the z-displacement (red) is representative of the effects of a finite-thickness sample and the y-displacement (green) is representative of rays collected from a sample with substantial bulk scattering.

Under certain iris and sample configurations, it is plausible that this scattering-dependent reduction in collected rays provides a non-unique likelihood mapping to a given ARS curve. Further investigation is recommended to assess the validity of this hypothesis and evaluate potential solutions. It is likely that a solution may be implemented as constraints placed upon the iris size and sample thickness for such experiments, or that the measured absorption fraction (measured by the photodiode power meters) may be included in the inversion method to uniquely identify a solution.

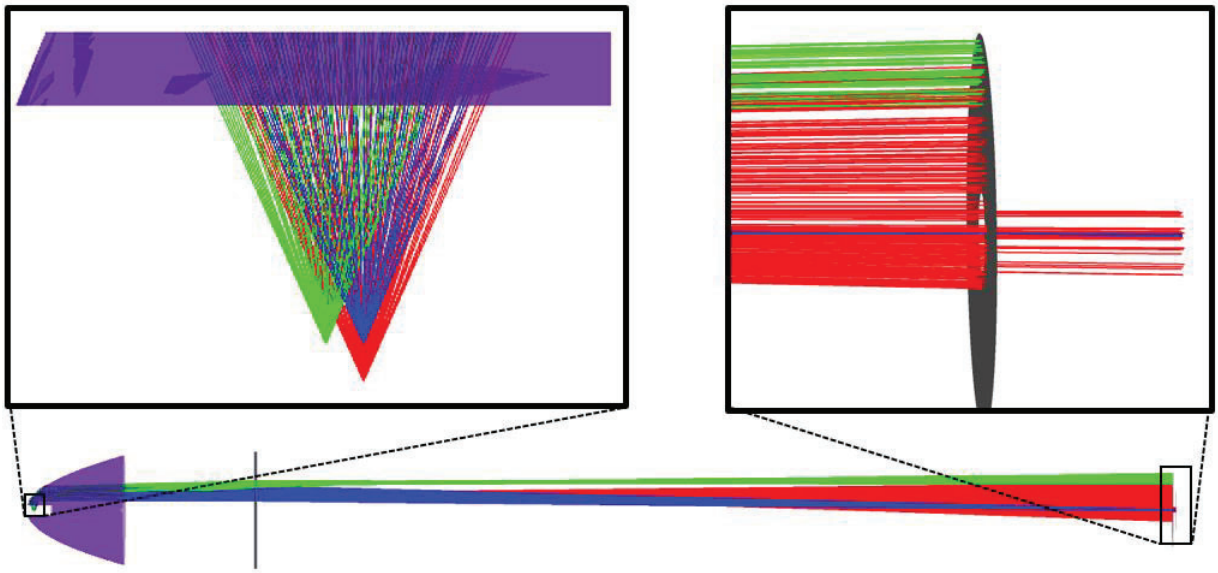

Figure 12. Simulation of the BOCS iris rejection of out-of-focus light

Addition of the BOCS weighting and detection raytracing methods to MCSLinv have reduced the error between the known and estimated optical properties of the Biomimic tissue phantom at 940 nm from the original MCSLinv code, however continued investigation and improvement to the methods and analysis is required for the BOCS to provide accurate estimates for μ_a and μ_s'. As

can be seen in Figure 13, the synthetic results for both the correct, known optical properties of the tissue phantom and the inversion result deviate significantly from the experimental dataset. One source of known error is that the scattering anisotropy and refractive index of the tissue are reported by the vendor at 660 nm while the μ_a and μ_s' are reported at 940 nm. The vendor (INO) provides μ_a and μ_s' characterization at additional wavelengths as a service – this would be prudent to pursue in the future for additional characterization (and was requested when the tissue phantom was originally ordered). Another potential source of error is the incomplete modeling of the BOCS system collection optics. The currently implemented strategy models the paraboloidal mirror, primary focusing lens, and iris, representing only a subset of the BOCS optical system. Modification of the MCSLinv software to include the entire collection optics system and image sensor could provide more representative synthetic datasets that would compare more favorably to the experimental datasets.

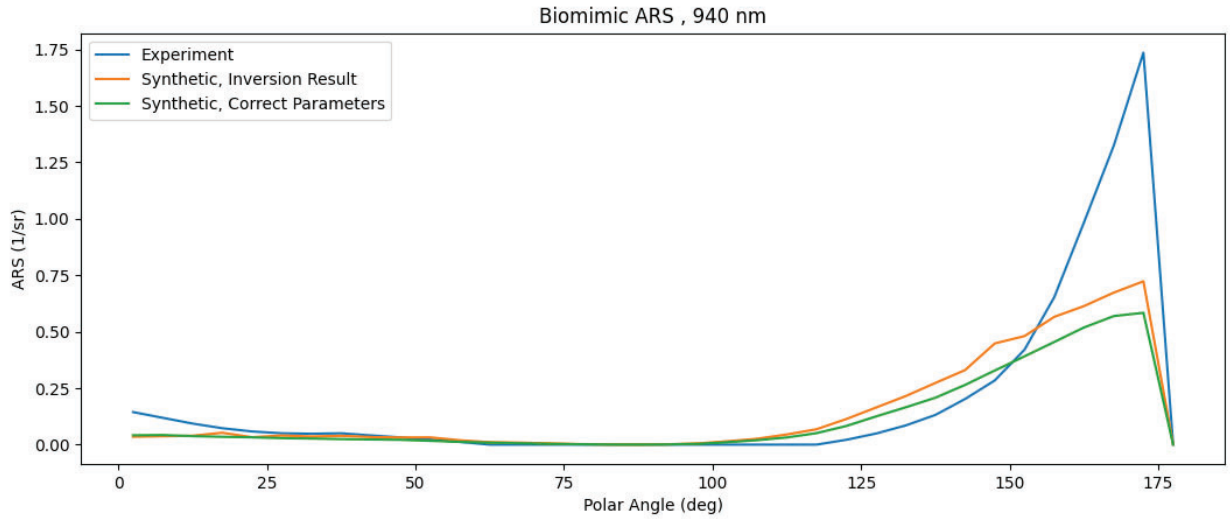

Figure 13. Experimental and synthetic Biomimic ARS datasets

3.3. Refractive Index Estimation

The BOCS measures the refractive index via first order ellipsometry, in which a series of BRDF measurements is captured as the beam's AOI is swept from approximately 40° to 65° while maintaining a P-polarization state at the sample plane. Note that this AOI range has been designed to cover the Brewster angle and surrounding angular regions for refractive indices of approximately 1.19 to 1.73 (in cases where the sample is surrounded by air). The resulting angle vs. reflectance curve is then used in an optimization routine to solve for the unknown refractive index in the Fresnel reflectance equation via minimization of the mean squared error (MSE) between the analytical solution and experimental data. A derived expression of the Fresnel equation for P-polarized reflectance (R_p) is shown in equation 8, where θ_i is the incident beam angle relative to normal, n_1 is the surrounding refractive index, and n_2 is the unknown medium's refractive index.

$$R_p = \left| \frac{n_1 \sqrt{1 - \left(\frac{n_1}{n_2} \sin\theta_i\right)^2} - n_2 \cos\theta_i}{n_1 \sqrt{1 - \left(\frac{n_1}{n_2} \sin\theta_i\right)^2} + n_2 \cos\theta_i} \right|^2 \quad \textbf{(8)}$$

Hardware polarization control is provided by a removable linear polarizer (LPVISC050, Thorlabs) and half wave plate (HWP) (AHWP05M-600, Thorlabs). As the beam's AOI is adjusted, the HWP is rotated using an electronic rotation stage (ELL14K, Elliptec) to maintain P-polarization at the sample plane. The correct rotation for each AOI is stored in a look-up-table (LUT), which is generated during calibration by iterating over all selected AOI in the scan sequence and minimizing the transmitted signal through a linear polarizer placed at the sample plane in the correct orientation (corresponding to the selected azimuth for AOI sweep). This calibration routine is only required during initial instrument setup or if the paraboloidal mirror or HWP are moved. During these measurements a linear polarizer is also placed in front of the BSDF measurement camera for improved contrast. The rotation of this polarizer is initially configured by maximizing the contrast of the Brewster angle attenuation in the reflected signal of a material with known refractive index.

During development of this measurement process, it was determined that even with the improvements made to the output power measurement system the accuracy was not sufficient for refractive index estimation. As such, an alternate approach was pursued in which the reflected signal from a protected aluminum mirror (PF10-03-G01, Thorlabs) was characterized and used to estimate the sample reflectance using the BSDF imagery. Use of an aluminum reference mirror enables estimation of an unknown sample's reflectance under identical conditions within the BOCS instrumentation, since the reflectance dependence on incidence angle is well documented and does not fall below 0.90 across the AOIs of interest [4]. For each mirror reference or sample image, a ROI corresponding to the known angular beam width – determined with the previously discussed beam width calibration – is used to identify the approximate specular component at a given angle of incidence. Using equation 9, the reflectance of a sample (R) is estimated using the integrated specular signal of the mirror calibration (I_m), the sample (I_s) and the known reflectance of the mirror under the given illumination conditions (R_c).

$$R = \frac{R_s}{R_m} R_c \quad \textbf{(9)}$$

Once the experimental reflectance curve is generated, the Fresnel reflectance function (equation 8) is used to solve for the unknown refractive index using Scipy's optimization tools [5] via minimization of the MSE between the experimental and synthetic data. To improve the quality of the fit, a Gaussian weighting function centered on the minimum value of the experimental data with standard deviation of 15° has been implemented, given that the most distinct feature in the measurable AOI range is that around the Brewster angle. An additional free parameter is included in the optimization routine that enables scaling of the entire experimental dataset by a scalar value between 0.05 and 1.0. This was implemented to accommodate for discrepancies in the amplitudes

of the analytical solution to the Fresnel equation and experimental data under certain instrument configurations (particularly with large beams, which tend to decrease contrast between the Brewster angle and the surrounding reflectance profile). However, use of this scaling parameter assumes correct identification of the Brewster angle within the experimental dataset as the minimum and can produce erroneous results if the sample is focused or highly diffuse. As such, a more robust calibration method would be a preferred approach.

Performance of the BOCS refractive index measurement is not yet robust enough with a single set of parameters to universally characterize all samples. For diffuse samples the region of interest around the beam must be reduced due to the blurring effect of the diffuse scattering, otherwise the fit is poor and will result in large refractive index errors. Another current limitation of this method is a high sensitivity to focus alignment between the mirror reference and sample. Intentionally defocusing a glass substrate from the nominal focus position by less than 80 μm was found to result in changes of up to 0.10 in the index estimate. This sensitivity is more problematic in diffusely reflecting samples (especially with non-flat surfaces) due to the inherent error in bringing them to focus. As such, extreme care is needed when aligning samples to the BOCS and evaluation of the measurement performance on a single point is advisable prior to performing a time-intensive scan. When correctly focused and optimized with suitable parameters, the approach can estimate the refractive index to within ±0.05 at 660 nm, as seen in Figure 14. A raw image produced via illumination of an N-BK7 glass sample with the beam directed at the Brewster angle is also shown in Figure 14, illustrating the reduction in reflectance observed by the BOCS within the experimental configuration.

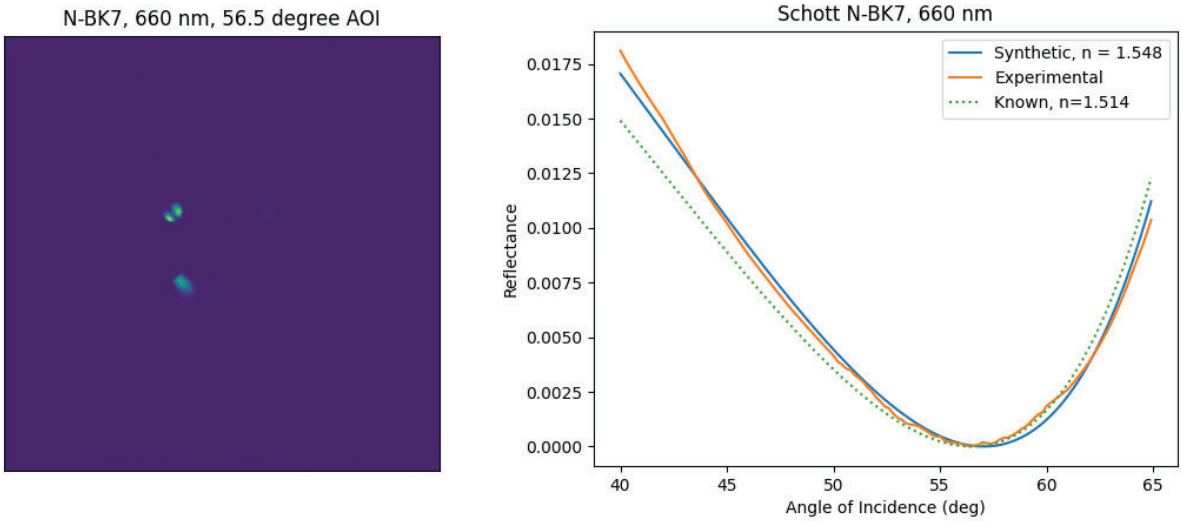

Figure 14. Brewster angle measurement and fit to the Fresnel reflectance equation

4.0 RESULTS AND DISCUSSION

4.1. BRDF

Validation of the BRDF measurement accuracy and repeatability was conducted via measurement of a ≈70% reflectance standard (Spectralon, Labsphere) and comparing to the known Lambertian profile. BRDF measurement results from the BOCS matched the known Lambertian profile within one standard deviation (from nine repeat measurements) across the entire 480 nm – 1100 nm spectral band.

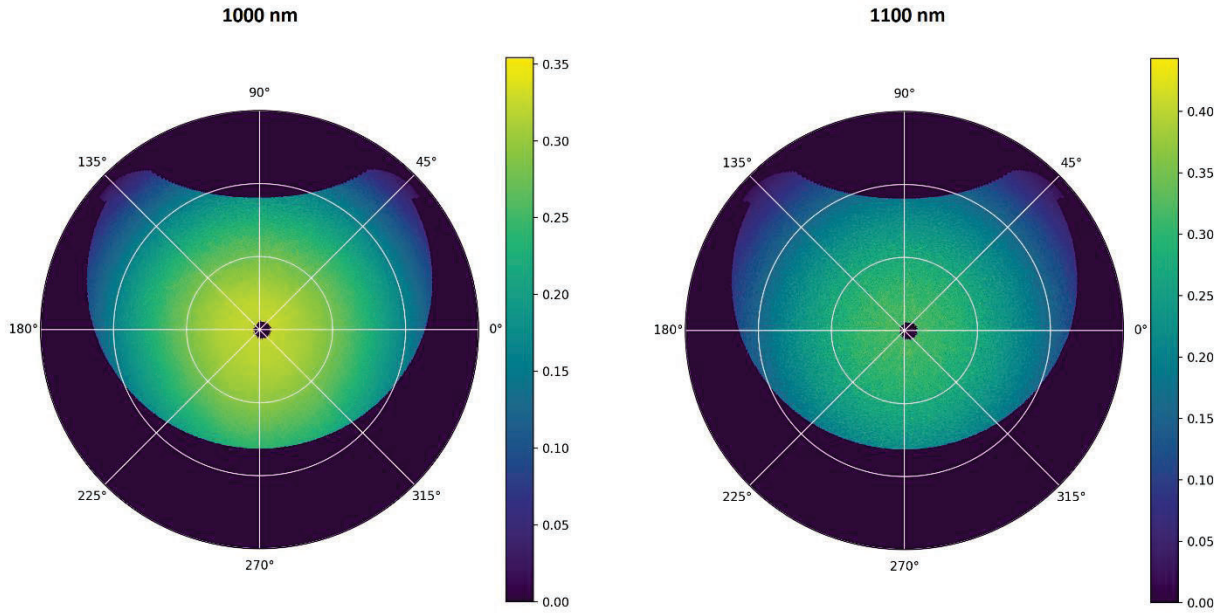

Figure 15. Polarimetric BRDF measurement data for the 70% reflectance standard

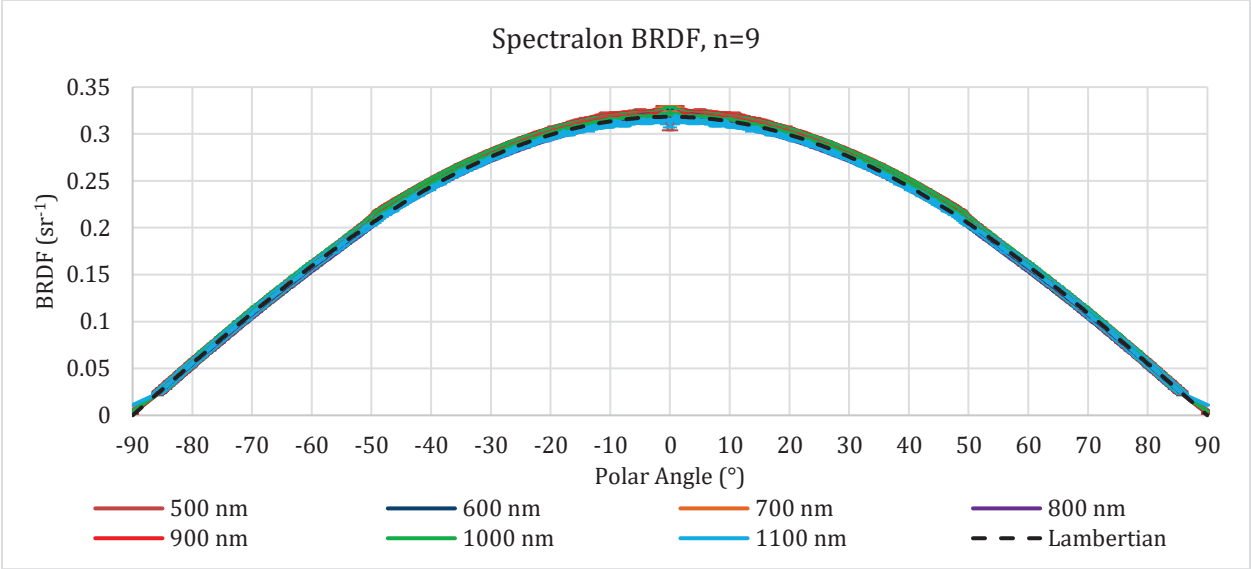

Figure 16. Multispectral BRDF measurements of the Spectralon reflectance standard

4.2. Reflectance, Transmittance, Absorbance

Validation of the BOCS reflectance, transmittance, and absorbance capabilities was performed via measurement of absorptive neutral density (ND) filters. Optical density values of 0.2 (NE02A, Thorlabs), 0.4 (NE04A, Thorlabs), and 1.0 (NE10A, Thorlabs) were characterized and compared to vendor-reported reflectance and transmittance data. Absorbance data was not provided by the vendor and as such was calculated from the reported reflectance and transmittance.

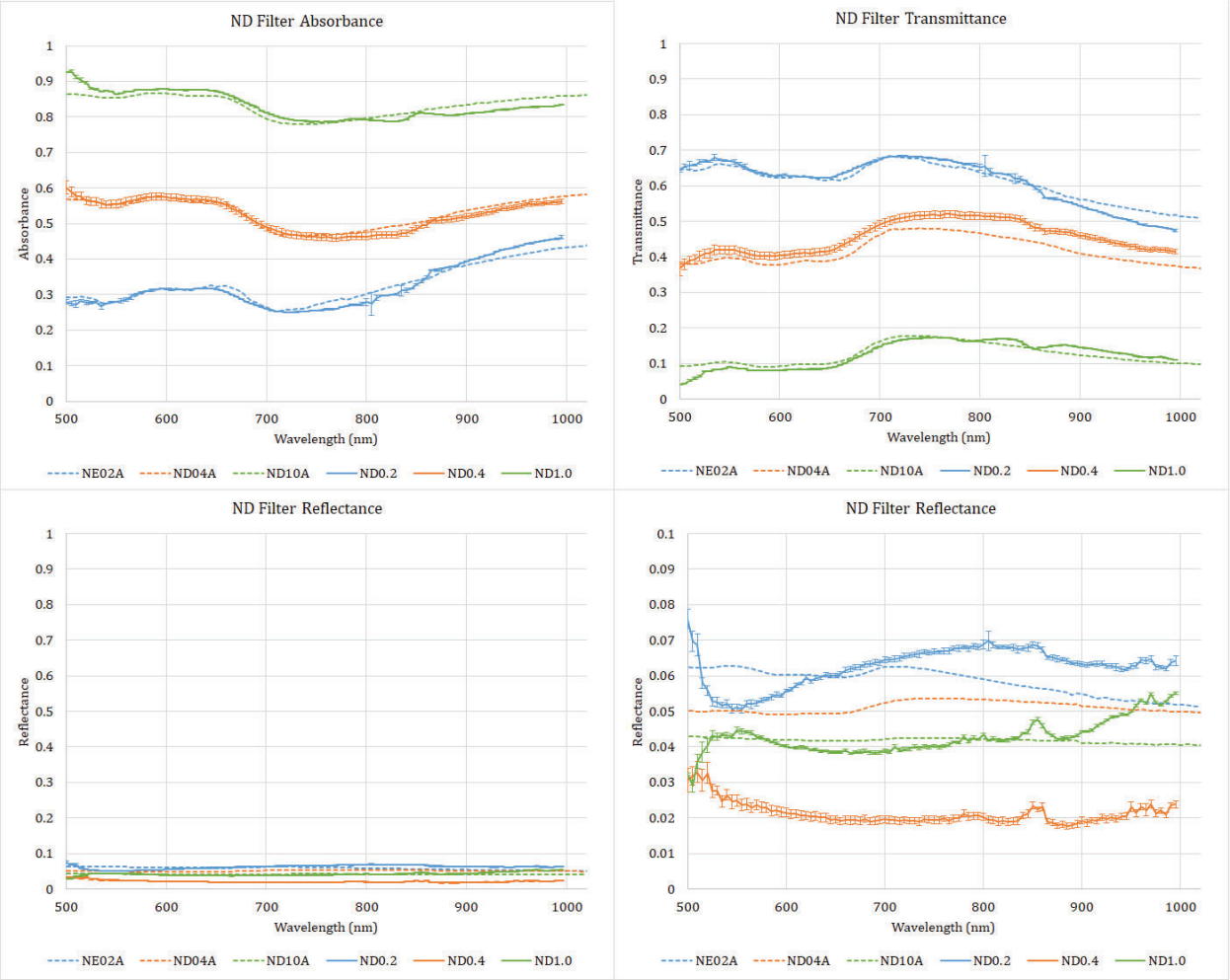

Figure 17. Measured ND filter absorbance, transmittance, and reflectance data

The redesign of the output photodiode measurement has improved these results from those performed during the Phase II effort. However, the worst-case accuracy demonstrated in these measurement (≈ 3.0%) is insufficient for estimating the refractive index. As such, alternative methods have been pursued.

4.3. Scattering and Absorption Coefficient

Scattering and absorption coefficient measurement performance validation was performed via characterization of a calibrated tissue phantom (Biomimic OP-HBO-C-940-0.65-5, INO). The tissue phantom consists of TiO_2 scattering particles and carbon black absorbing dye that are blended into a polyurethane base to achieve the desired optical properties. The vendor reported optical properties are shown in Table 1. Note that these reported properties were characterized at 940 nm and not 1064 nm due to limitations with the vendor's characterization capabilities.

Parameter	Symbol	Value	Wavelength
Reduced Scattering Coefficient	μ_s'	5.23 cm^{-1}	940 nm
Scattering Coefficient	μ_s	13.76 cm^{-1}	-
Absorption Coefficient	μ_a	0.84 cm^{-1}	940 nm
Henyey-Greenstein Scattering Anisotropy	g	0.62 ± 0.015	660 nm
Refractive Index	n	1.521 ± 0.006	660 nm
Thickness (nominal)	t	0.5 mm	-

Table 1. INO Biomimic OP-HBO-C-940-0.65-5 Tissue Phantom properties

Measurement of the Biomimic tissue phantom using the BOCS did not produce results consistent with the vendor-reported absorption (μ_a) and scattering (μ_s') coefficients. Initial results indicated a dramatic overestimation of μ_a and μ_s', which prompted a detailed investigation into the cause of these discrepancies as well as potential solutions. These investigations are summarized in section 3.2 above. The μ_a and μ_s' estimation with the current BOCS measurement and software configuration is not yet validated.

4.4. Scattering Anisotropy

The Henyey-Greenstein scattering anisotropy factor was validated by measurement of the same calibrated tissue phantom used for validation of the scattering and absorption coefficients (Biomimic OP-HBO-C-940-0.65-5, INO). This tissue phantom has a vendor reported scattering anisotropy factor of 0.62 ± 0.015 at 660 nm, and as such was used to validate the measurement. The resulting dataset generated by the BOCS agrees with the calibrated value within the measurement and reported error, as seen in Figure 18. Discussions with the tissue phantom vendor indicated that they provide characterization at additional wavelengths as a service; characterization of the tissue phantom by the vendor at more wavelengths would be beneficial to assess the broadband accuracy of this measurement.

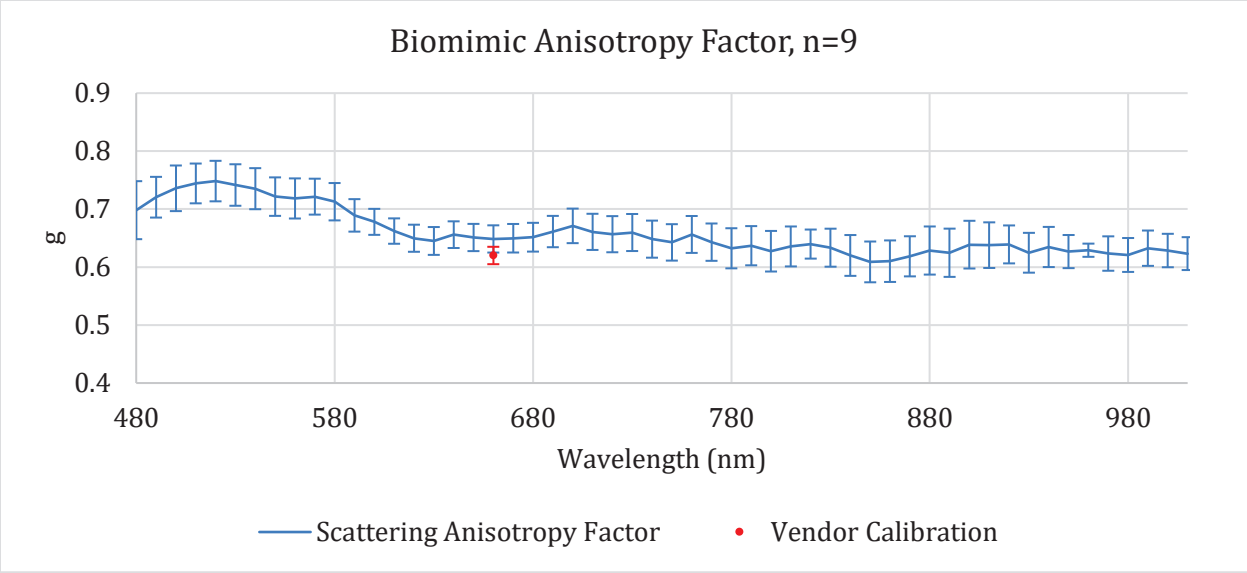

Figure 18. Henyey-Greenstein scattering anisotropy validation data

4.5. Refractive Index

The refractive index measurement capability was validated via measurement of a calibrated tissue phantom (Biomimic OP-HBO-C-940-0.65-5, INO), which has a known refractive index of 1.52 ± 0.006 at 660 nm. The index reported from BOCS estimates was 1.55 ± 0.017 for a sample size of five, which represents an error of 0.03. The raw experimental data, as well as the optimized result of the fitting of the data to the Fresnel reflectance equation is shown in Figure 19. Additional characterization of materials with known indices across a wider spectral band should be performed to fully validate this capability.

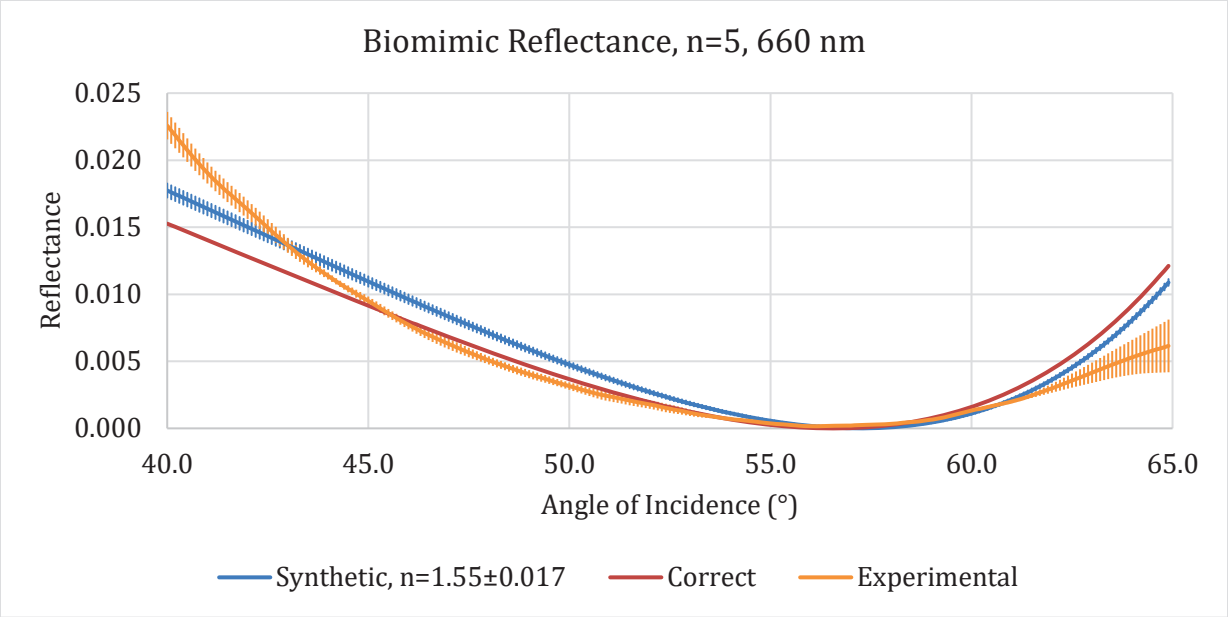

Figure 19. Biomimic tissue phantom refractive index measurement data

5.0 CONCLUSIONS

Improvements made to the BOCS under this effort have advanced the technology closer to the readiness level needed to perform measurements as a research tool, and validation measurements performed under this effort on a subset of the BOCS capabilities such as BRDF, refractive index, and Henyey-Greenstein scattering anisotropy factor indicate that the accuracy and repeatability of the system are approaching the project goals of being able to accurately measure the optical properties of turbid media, including biological tissue. Issues with the calibration standard purchased to support this validation effort likely negatively impacted the assessment of the devices ability to measure absorption and reduced scattering coefficients. Researchers at the Bioeffects Division struggled to measure the optical property values for this standard using integrating sphere spectroscopy and inverse adding doubling that match the manufacturer advertised values. The thin nature of the calibration standard could have negatively impacted the ability to accurately make measurements.. For the measurement capabilities that did produce accurate results a larger variety of samples should be measured for improved validation confidence.

Unfortunately, due to unexpected complications with the scattering and absorption measurement process the program budget was expended before being able to complete the full system validation and planned tissue experiments. Primarily, the resulting μ_a and μ_s' estimates produced by the BOCS on a calibrated tissue phantom do not compare favorably to those reported by the vendor. Nanohmics has several hypotheses and mitigation strategies that may be pursued in the future to identify the cause of these discrepancies. Progress made on the refractive index measurements has enabled estimation of sample properties to within ±0.03 but further refinement to the analysis software and experimental methods using a larger set of samples is recommended prior to employing the capability for use as a research tool, as the sample set was limited to only the Biomimic tissue phantom and a glass substrate (N-BK7, Schott).

In summary, with the array of improvements implemented within the BOCS hardware, software, and calibration methods the system has advanced towards full validation as a research instrument and tool. However, Nanohmics recommends further development, particularly on the scattering and absorption coefficient measurement capabilities, as well as validation of the other measurands on a larger sample set prior to use for scientific studies.

6.0 REFERENCES

[1] Z. J. Ren J, "Measurement of a bidirectional reflectance distribution and system achievement based on a hemi-parabolic mirror," *Optics Letters,* vol. 35, no. 9, pp. 1458-1460, 2010.

[2] Z. Levine, "MCSLinv," National Institute of Science and Technology, 20 Sep 2017. [Online]. Available: https://github.com/usnistgov/MCSLinv. [Accessed 2021].

[3] Z. S. R. L. A. P. A. C. C. L. P. Levine, "Algorithm for rapid determination of optical scattering parameters," *Optics Express,* vol. 25, no. 22, pp. 26728-26746, 2017.

[4] E. G. Kashif Islam, "Multi-LED light source for hyperspectral imaging," *Optics Express,* vol. 25, no. 26, pp. 32659-32668, 2017.

[5] R. G. T. E. O. M. H. Pauli Virtanen, "SciPy 1.0: Fundamental Algorithms for Scientific Computing in Python," *Nature Methods,* vol. 17, no. 3, pp. 261-272, 2020.

LIST OF SYMBOLS, ABBREVIATIONS, AND ACRONYMS

ADC	Analog to Digital Converter
AFRL	Air Force Research Laboratory
AOI	Angle of Incidence
ARS	Angle Resolved Scattering
BOCS	Broadband Optical Characterization System
BRDF	Bidirectional Reflectance Distribution Function
BSDF	Bidirectional Scatter Distribution Function
BTDF	Bidirectional Transmittance Distribution Function
FPA	Focal Plane Array
HEL	High Energy Laser
HWP	Half Wave Plate
LUT	Look Up Table
MCSLinv	Inverse Monte Carlo Solver (NIST software package)
MSE	Mean Squared Error
ND	Neutral Density (optical filter)
NIR	Near Infrared
NIST	National Institute of Standards and Technology
OD	Optical Density
ROI	Region of Interest
RHDO	Optical Radiation Bioeffects branch
STARR	Spectral Tri-function Automated Reference Reflectometer